

# Two-dimensional many-body localized systems coupled to a heat bath

Joey Li,<sup>1,2</sup> Amos Chan,<sup>3</sup> and Thorsten B. Wahl<sup>4</sup>

<sup>1</sup>*Institute for Theoretical Physics, University of Innsbruck, 6020 Innsbruck, Austria*

<sup>2</sup>*Institute for Quantum Optics and Quantum Information of the Austrian Academy of Sciences, 6020 Innsbruck, Austria*

<sup>3</sup>*Department of Physics, Lancaster University, Lancaster LA1 4YB, United Kingdom*

<sup>4</sup>*TCM Group, Cavendish Laboratory, Department of Physics,  
J J Thomson Avenue, Cambridge CB3 0HE, United Kingdom*

(Dated: October 21, 2024)

We numerically investigate the effect of coupling a two-dimensional many-body localized system to a finite heat bath, using shallow quantum circuits as a variational ansatz. Specifically, we simulate optical lattice experiments with two components of ultracold bosons, where only one species is subject to a random disorder potential and the other acts as a heat bath. We obtain a filling fraction-dependent phase diagram with a critical filling consistent with experiments. We also calculate two-point correlation functions and the quantum mutual information between sites. We observe a distribution of the quantum mutual information in the many-body localized regime which is consistent with the presence of resonances, similar to those observed in one-dimensional many-body localized systems.

## I. INTRODUCTION

The assumption that isolated systems act as their own heat baths and therefore reach thermal equilibrium was largely taken for granted until the beginning of this century when several analytical [1, 2] and numerical works [3, 4] started to provide evidence for the existence of many-body localization (MBL). Experiments observing MBL [5–9] and a rigorous proof [10] in the last decade seemed to put the phenomenon on solid ground. However, in recent years, multiple works started questioning the existence of true MBL [11–13], even in one dimension. This would imply that MBL in one dimension is only a transient effect (as has long been conjectured for higher dimensions [14, 15]), though on incredibly long time scales.

Extremely long thermalization times imply that strongly disordered isolated quantum systems behave many-body localized on experimentally relevant time scales. That is, for all practical purposes one can assume the existence of MBL, even in higher dimensions, where it has also been experimentally observed [16]. In this spirit, we investigate the effect of coupling a localized and delocalized system in higher dimensions, a subject that is relevant for the understanding of thermalization phenomena and time scales. In particular, we study a two-dimensional “MBL-like” system coupled to a heat bath, and aim to reproduce the phase transition point found in two-dimensional optical lattice experiments with two-component ultracold bosons [17] as the size of the heat bath is increased. In those experiments, one boson species was subject to random disorder while the other only experienced the optical lattice potential, acting as a heat bath for the former.

We use quantum circuits, a type of tensor networks, as a variational ansatz for our classical simulations. Shallow quantum circuits have proven useful for both the numerical description of one- [18–20] and two-dimensional MBL systems [21–23] and the rigorous classification

of symmetry-protected topological MBL phases [24–26]. We optimize a two-dimensional shallow quantum circuit to approximately diagonalize a hardcore version of the Hamiltonian modelling the experiments of Ref. [17]. The unitaries building up the quantum circuit contain the variational parameters of the approach. After optimizing those, we have an approximate representation of the overall unitary diagonalizing the Hamiltonian and can extract local features (such as correlations) of its eigenstates. We analyze entanglement features in the different particle sectors of the diagonalizing unitary to obtain the phase diagram as a function of the disorder strength and the fraction of bosons not experiencing the disorder potential. [Note that we use the semantics of a phase transition throughout this work, although transience of MBL implies that instead we have a (relatively sharp) crossover between a regime of extremely slow, experimentally inaccessible thermalization and fast thermalization.] We obtain a phase transition point in the same regime as the measured value. We also extract the correlation lengths from our optimized unitaries, which show a slow decay with disorder strength. Finally, we find that the quantum mutual information distributions between sites separated with short and medium distances develop longer tails as the disorder strength is lowered towards the transition point. This indicates that resonances might be at play on experimentally relevant time scales near the transition in higher dimensions, similar to one dimensional MBL [27].

## II. MODEL AND NUMERICAL APPROACH

We study a two-dimensional MBL system coupled to an immersed heat bath. Specifically, we consider two components of bosons confined by an optical square lattice. One species of bosons (“dirty bosons”) experiences a randomly chosen on-site disorder potential while the other one (“clean bosons”) acts as a heat bath. We assume that the dynamics of the bosons is governed by the

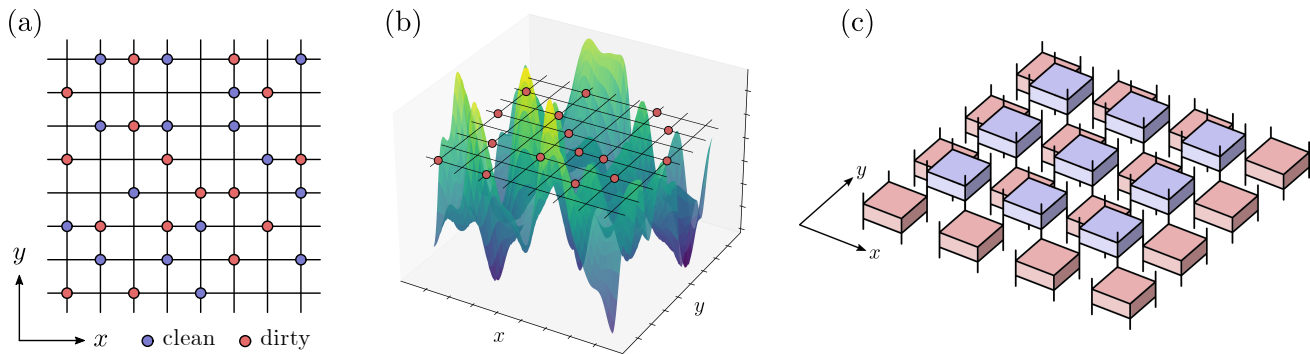


FIG. 1. (a) Optical lattice filled with two species of bosons: “clean” (blue) and “dirty” (red). Half the lattice sites are occupied: the overall filling is  $\nu = 0.5$ . We consider various relative fractions  $f_c$  and  $f_d$  of clean and dirty particles: depicted here is the case  $f_c = f_d = 0.5$ . (b) The system is in a random potential that affects *only* the dirty particles. (c) Two-layer quantum circuit  $U$  used as a variational ansatz to approximately diagonalize the Hamiltonian.

Hamiltonian of Ref. [17],

$$H_{\text{exp}} = -J \sum_{\langle i,j \rangle, \sigma} a_{i,\sigma}^\dagger a_{j,\sigma} + \frac{V}{2} \sum_{i,\sigma} n_{i,\sigma} (n_{i,\sigma} - 1) + V \sum_i n_{i,d} n_{i,c} + \sum_i \delta_i n_{i,d}, \quad (1)$$

where  $i = (x, y)$  denotes the lattice site.  $J$  is the tunneling amplitude, i.e., hopping strength,  $V$  the on-site repulsion strength, and  $\delta_i$  the random disorder potential, which is chosen according to a Gaussian distribution with half-maximum width  $\Delta$ . We consider only bosons in the center of the optical trap, where the trap potential can be neglected.  $a_{i,\sigma}$  denotes the annihilation operator of a boson at site  $i$  for  $\sigma \in \{c, d\}$  with  $c$  ( $d$ ) corresponding to clean (dirty) bosons and  $n_{i,\sigma} \equiv a_{i,\sigma}^\dagger a_{i,\sigma}$  the corresponding particle number operator. See Fig. 1 for an illustration.

In numerical simulations, one typically has to truncate the on-site occupation number of bosons, which can in principle be arbitrarily large. As experimentally only doublon fractions of up to 16% are observed [17] (due to the large on-site repulsion of  $V = 24.4J$ ) and to make our simulations numerically feasible, we restrict ourselves to hardcore bosons. Our Hamiltonian becomes

$$H = -J \sum_{\langle i,j \rangle, \sigma} a_{i,\sigma}^\dagger a_{j,\sigma} + \sum_i \delta_i n_{i,d}. \quad (2)$$

We note that due to the (infinite) on-site repulsion, this Hamiltonian still describes an interacting model.

Introducing a two-layer quantum circuit  $U$  [21–23] [see Fig. 1(c)] as an ansatz, we variationally diagonalize the Hamiltonian (2) via numerical optimization of  $U$  such that  $UHU^\dagger$  is approximately diagonal. To that end, we minimize a cost function which is a sum of local tensor network contractions. For details, see Appendix A. The constituting unitary gates encode all (approximate) eigenstates of the Hamiltonian. Since the Hamiltonian (2) preserves the particle numbers of both

clean and dirty bosons, its eigenstates also have fixed clean and dirty particle numbers. We impose this at the level of the individual unitaries building up the quantum circuit in our numerical approach [21, 22]; see Appendix A. This makes it straightforward to access individual particle sectors of our overall unitary.

We note that the approximate eigenstates encoded in our unitary  $U$  represent the dynamics of the Hamiltonian  $H$  on short time scales: it does not make a significant difference whether we consider the exact evolution of an initial state  $|\psi_0\rangle$  via  $|\psi(t)\rangle = e^{iHt}|\psi_0\rangle = U_{\text{exact}} e^{iE_{\text{exact}}t} U_{\text{exact}}^\dagger |\psi_0\rangle$  or the approximate evolution  $|\tilde{\psi}(t)\rangle = U e^{iEt} U^\dagger |\psi_0\rangle$ , as long as the time  $t$  is small. (Here  $E_{\text{exact}} = U_{\text{exact}}^\dagger H U_{\text{exact}}$  is the diagonal matrix of the exact energies, and  $E$  is the diagonal matrix of the variational energies of the approximate eigenstates encapsulated in  $U$ .) Hence, if the approximate eigenstates are close to the exact ones (at least in the particle sector of  $|\psi_0\rangle$ ),  $U$  gives a correct picture of short time-scale behavior, such as experimentally measured transition points. For details on this argument, we refer the reader to Ref. [22].

Once the optimized unitaries have been obtained, we can calculate one- and two-point functions of the approximate eigenstates (see Appendix B). For the purpose of producing the phase diagram, we estimate the location of the transition (technically, crossover) point by using the fact that the variation of entanglement in the system between different disorder realizations is greatest at the critical disorder strength [28]. Specifically, the process is as follows: one can extract the on-site entanglement entropies with respect to sites  $i$ . After averaging over eigenstates in particle sectors and calculating the fluctuation with respect to disorder realizations, one obtains maxima around the phase transition point [19, 20, 22, 23, 28]. (To improve numerical stability, in the final step, one also averages the entanglement entropy fluctuation over sites  $i$ .) The disorder strengths  $\Delta$  where these maxima are located can be used to extract the phase transition points. We

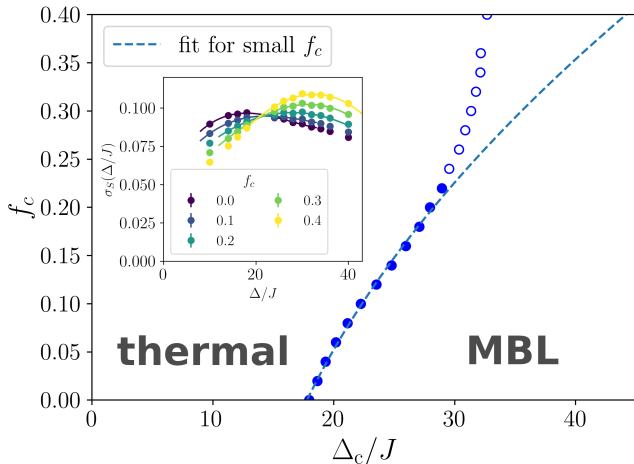


FIG. 2. Phase diagram of thermal and MBL-like regimes for overall filling fraction  $\nu = 0.5$  obtained by extracting the transition points from the maxima in the inset. The dashed line indicates a second order polynomial fit to our data for small  $f_c$  (filled circles), from which our method deviates for  $\Delta \gtrsim 30J$  (empty circles). Inset: Entanglement entropy fluctuation (see main text) as a function of disorder strength  $\Delta$  with fractions  $f_c$  of clean particles as indicated in the legend. The error bars (evaluated as in Ref. [22]) are smaller than the symbol size.

carry out this analysis for overall filling fraction  $\nu = 0.5$  as in the experiment [17] and as a function of the fraction  $f_c \in [0, 1]$  of clean bosons, by explicitly selecting approximate eigenstates with the desired values of  $\nu$  and  $f_c$ . For our simulations, we consider the Hamiltonian as defined on a  $10 \times 10$  lattice with periodic boundary conditions, i.e., we have  $N_c + N_d = 50$  bosons.

### III. RESULTS

Here we present our results on the phase diagram as a function of the fraction  $f_c$  of clean particles, the correlation functions, and the quantum mutual information.

#### A. Clean particle fraction-resolved phase diagram

In Fig. 2 we show the numerical data obtained by optimizing our quantum circuit ansatz for 30 disorder realizations as a function of disorder strength  $\Delta$ . To increase numerical stability, we used the same 30 disorder profiles for all  $\Delta$  and only varied the overall prefactor [19, 21, 22]. As detailed above, we calculated the fluctuation of the eigenstate-averaged (sampling over 4000 approximate eigenstates) on-site entanglement entropy with respect to disorder realizations and averaged the result over the site positions. We restricted the eigenstates to have  $N_c + N_d \equiv N_{\text{tot}} = 50$  bosons with  $N_c/N_{\text{tot}} = f_c$  fixed. The corresponding filling fraction-resolved entan-

glement entropy fluctuation is shown in Fig. 2. For all fractions  $f_c$  of clean particles, we find a maximum in the entanglement entropy fluctuation, whose disorder strength value we used to plot the filling-fraction dependent MBL-thermal phase diagram. We note that for disorder strengths  $\Delta \gtrsim 30J$  our phase boundary deviates from the expected behavior of approaching the  $f_c = 1$  line asymptotically. Such a behavior is required, as the eigenstates for any arbitrarily large  $\Delta$  are always delocalized if  $f_c$  is close enough to 1, such that the  $N_d = (1 - f_c)N_{\text{tot}}$  dirty bosons cannot localize the clean ones. As a result, Taylor expansion of  $f_c(\Delta_c)$  should have a negative coefficient in second order. We fit our data to such a second order polynomial in the regime where the data points follow a curve which is right-bent. Crucially, the transition point  $\Delta_c(f_c = 0) = 18J$  is consistent with Ref. [21], i.e., the small  $f_c$  results are reliable. Specifically, they match the expected (fitted) behavior in the range  $0 \leq \Delta_c(f_c) \leq 30J$ , which covers the experimental value of  $\Delta = 28J$  [17]. For the experimental disorder strength, we find a transition at  $f_c \approx 0.2$ , which compares favorably with the experimental value of  $f_c^{\text{exp}} = N_c/N_{\text{tot}} \approx 40/(124 \pm 12) \approx 0.3$  [17] given the simplicity of our approximation. This underpins the statement that, due to their local structure, shallow quantum circuits are capable of capturing the transition points found with charge-density-wave imbalance experiments [22]. The still significant deviation from the experimental value is mostly due to two reasons: On the one hand, the unitaries building up our quantum circuit act only on plaquettes of  $2 \times 2$  sites, which limits the amount of entanglement allowed by our ansatz. On the other hand, we considered a hardcore Bose-Hubbard model, i.e., we neglected double and higher occupancies. Mitigating either of these restrictions would likely lead to a transition point closer to the experimental one, but would require vastly larger computational resources.

#### B. Two-point correlation function

Our method also allows us to use the optimized unitaries to calculate two-site reduced density matrices (see Appendix B for details), from which we can compute two-point correlation functions and the quantum mutual information (QMI) between sites.

We first consider correlation functions. Within our approximation, the two-site correlation function  $C_{\sigma\mu}(i, j) = \langle n_{i,\sigma} n_{j,\mu} \rangle - \langle n_{i,\sigma} \rangle \langle n_{j,\mu} \rangle$ , with  $\sigma, \mu \in \{c, d\}$ , is non-trivial only in a fixed range of separations between sites  $i$  and  $j$  (causal) cone. The obtained correlations and extracted correlation lengths are shown in Fig. 3. We note the slow decay of the average correlation lengths with disorder strength  $\Delta$ , cf. Ref. [21]. Furthermore, we find that the correlation lengths for dirty and clean particles are very similar, indicating that the dirty particles are effective at localizing the clean ones in the MBL regime within our approximation. For example, for  $f_c = 0.2$  we observe

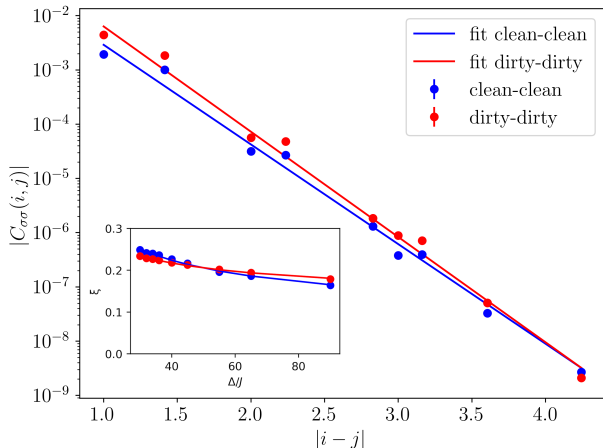


FIG. 3. Decay of correlations as a function of distance  $|i - j|$ , shown for the example of  $\Delta = 36J$ . The data were obtained by averaging over 100 randomly chosen approximate eigenstates with fraction  $f_c = 0.2$  of clean bosons and averaging over 30 disorder realizations. Error bars denote fluctuations between disorder realizations and are smaller than the symbol size. For the fits, we used linear functions after taking the logarithm for the three data points of smallest distance. Inset: Correlation lengths extracted from the fits as shown in the main figure for various values of  $\Delta$  and  $f_c = 0.2$ . The solid lines denote  $1/\ln(\Delta/J)$  fits [29–31].

that  $\overline{\xi_{cc}}(\Delta = 45J) = 0.22 \pm 0.01$  and  $\overline{\xi_{dd}}(\Delta = 45J) = 0.21 \pm 0.01$ , decaying to  $\overline{\xi_{cc}}(\Delta = 90J) = 0.16 \pm 0.01$  and  $\overline{\xi_{dd}}(\Delta = 90J) = 0.18 \pm 0.01$ . Our predictions for the two-point correlations can be compared to future optical lattice experiments.

### C. Quantum mutual information

Finally, we consider the quantum mutual information (QMI), which has been used to quantify correlations in MBL systems [32, 33], and more recently has been studied in the context of resonances [34]. Here, we study the distribution of the QMI between individual sites in our two-dimensional model (2). The QMI of an eigenstate  $|\psi\rangle$  is defined as

$$I(A : B) = S(\rho_A) + S(\rho_B) - S(\rho_{AB}), \quad (3)$$

where the system is partitioned into three disjoint parts  $A$ ,  $B$ ,  $C$ , and the QMI is between regions  $A$  and  $B$ .  $\rho_X$  is the reduced density matrix of  $|\psi\rangle$  obtained by tracing out its complement  $\overline{X}$ ,

$$\rho_X = \text{tr}_{\overline{X}}(|\psi\rangle\langle\psi|), \quad (4)$$

and  $S(\rho_X) = -\text{tr}(\rho_X \ln(\rho_X))$  denotes the von Neumann entropy.

We first review the expected behavior of the eigenstate QMI probability distribution. In general, the two-site QMI  $I(i : j)$  decays exponentially with distance in

the MBL regime, and decays more slowly in the thermal regime [32]. The probability distribution of values of the two-site QMI in thermal-regime eigenstates is roughly symmetric and centers around a value independent of the distance  $|i - j|$ , while in the MBL regime, the QMI distribution is more one-sided with greatest probability near zero, but also longer tailed, with more instances of near-maximal QMI, particularly for small  $|i - j|$  [33]. When considering the QMI distributions at various disorder strengths, the distribution is expected to be independent of disorder strength for neighboring sites, while for large  $|i - j|$  the distribution is more heavily centered around 0 at very strong disorder, and longer tailed closer to the transition point.

Using our variational method, we calculate the QMI, from the two-site reduced density matrices (which can be obtained as illustrated in Appendix B), sampling over 100 approximate eigenstates per disorder realization and disorder strength. As our ansatz only captures area law-entangled states, we are unable to study the QMI distribution in the thermal regime. The results, for disorder strengths at the transition point and above, are shown in Fig. 4. We note that although the local Hilbert space dimension of this model is 3, the maximum QMI between two sites is  $I(i : j) = 2 \ln 2$ , equivalent to that of two maximally entangled qubits, as particle number conservation prohibits the existence of maximally entangled two-qutrit states on a subsystem of two sites.

As our approximation only captures non-trivial correlations within a fixed range of distances, we can only consider certain separations between sites  $i$  and  $j$ . We consider the short-ranged, i.e. nearest-neighbor case in Fig. 4(a), where the distributions are roughly similar for different disorder strengths and show instances of near-maximal QMI, as expected based on analogous studies in one-dimensional MBL. We also consider the “medium-ranged” case in Fig. 4(b) and (c). We are unable to consider the long-ranged case, as, within our approximation, sites are uncorrelated for  $|i - j| > 3\sqrt{2}$ . In addition, a further limitation arising from the local nature of the ansatz is that the QMI is consistently  $\lesssim 0.2$  for  $|i - j| \geq 2$  and  $\lesssim 0.05$  for  $|i - j| > 3$ , independently of the model under consideration. Thus in Fig. 4(b) and (c), the observed values of the QMI are likely significantly below the true values. However, the qualitative aspects of these plots may still capture some of the relevant physics. This is because each approximate eigenstate is essentially the projection of an exact eigenstate onto a manifold of weakly entangled states; since the projection is the same in all cases, it is still meaningful to consider *relative* differences, especially correlations or related quantities between different sets of eigenstates. In particular, this allows us to compare the two-site QMI, at fixed distances, between the system at different disorder strengths.

We now discuss the relation to resonances, which have been suggested to be the driving force behind the transition from the MBL to the thermal regime in one dimension [27, 34–37]. Resonances can be viewed as superposi-

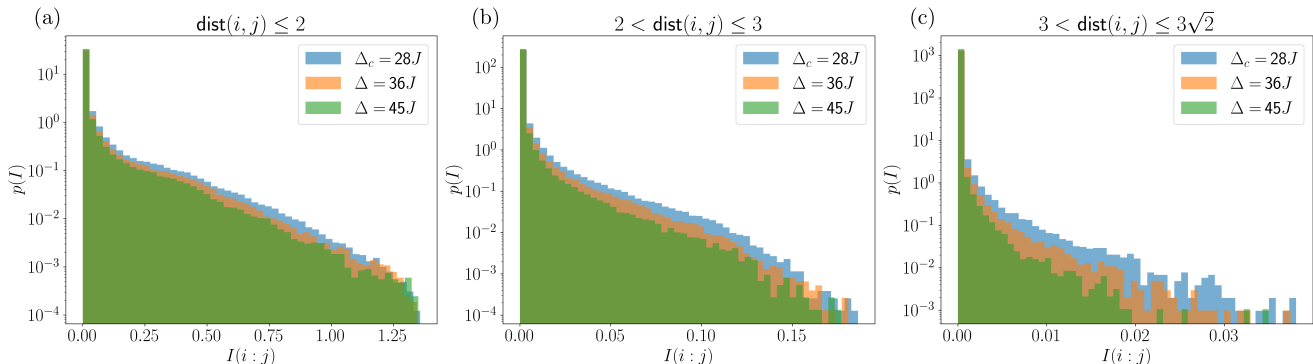


FIG. 4. Probability density of the two-site QMI obtained by sampling over 100 eigenstates and 30 disorder realizations, taking all sites into account, for  $f_c = 0.2$  (corresponding to a transition point  $\Delta_c = 28J$ ) and the values of  $\Delta$  indicated in the legend. The distances between the sites are  $\text{dist}(i, j) \leq 2$  in (a),  $2 < \text{dist}(i, j) \leq 3$  in (b), and  $3 < \text{dist}(i, j) \leq 3\sqrt{2}$  in (c).

tions of few (deep in the MBL regime, two) near-product states whose local occupations differ in many sites, e.g., cat states. A crucial requirement is that those superpositions are the result of the near-product states having hybridized due to them being close in energy. This can be detected via the QMI if the regions  $A$  and  $B$  (in our case, sites  $i$  and  $j$ ) are far away (typically of the order of the system size), such that a non-vanishing QMI indicates the superposition of macroscopically distinct near-product states, which, due to the locality of the Hamiltonian, must be close in energy [34]. Due to the locality of our ansatz, we are unable to detect such long-range resonances. However, we are able to get some indication of the appearance of resonances by studying how the QMI between the most distant sites accessible builds up as the disorder strength  $\Delta$  is lowered towards the transition.

We observe that in Fig. 4(c) the distribution of the QMI develops tails near the transition that are absent for larger  $\Delta$ . We note that the lengths of these tails are constrained due to the aforementioned limitations arising from the short range nature of the ansatz. We do not observe the near-maximal QMI that is the hallmark of many-body resonances, in the “medium-ranged” case. However, the qualitative behavior of the distribution is reminiscent of the expected behavior of the distribution of the longer-range QMI as the disorder strength is lowered towards the transition point. Although we do not directly capture resonances, within the range of QMI and site separations that we do capture, we observe a broadening in the QMI distribution with decreasing  $\Delta$  that is consistent with the increased presence of resonances near the transition point, analogous to the one-dimensional case.

#### IV. CONCLUSIONS

We used quantum circuits to simulate a two-component ultracold bosonic gas, where one component is localized by a disorder potential and the other acts as

a heat bath. We found a transition point of the fraction of clean particles in the same regime as the experiments of Ref. [17]. We also calculated the correlation lengths as quantities to be compared to future experiments. Finally, we computed the QMI of our approximate eigenstates as a signature of rare resonances. We found that the distribution of the QMI gets broader as the disorder strength is decreased towards the transition. This is consistent with the perspective that the proliferation of resonances contributes to the two-dimensional MBL-to-thermal crossover seen on experimental time scales – analogous to the case in one dimension. Further studies are required to confirm this hypothesis.

#### ACKNOWLEDGMENTS

We thank David Huse for helpful discussions. JL acknowledges support from ERC Starting grant QARA (Grant No. 101041435) and the Austrian Science Fund (FWF): COE 1 and quantA. AC acknowledges support from the Royal Society grant RGS\R1\231444 and from the EPSRC Open Fellowship EP/X042812/1. TBW acknowledges funding from an EPSRC ERC underwrite grant EP/X025829/1.

#### Appendix A: Variational ansatz

In this work, we use the quantum circuit  $U$ , a two-layer tensor network with the structure depicted in Fig. 1(c), to variationally diagonalize the Hamiltonian (2), i.e. approximately calculate the full set of eigenstates. (More precisely, only a subset of the tensor network is depicted in Fig. 1(c), for clarity. Since we consider an  $L \times L = 10 \times 10$  system in our numerics, both the lower layer and upper layer consist of  $5^2$  tensors, with the tensors on the edges connected as prescribed by periodic boundary conditions.)

$U$  may also be recast as a large matrix in the full

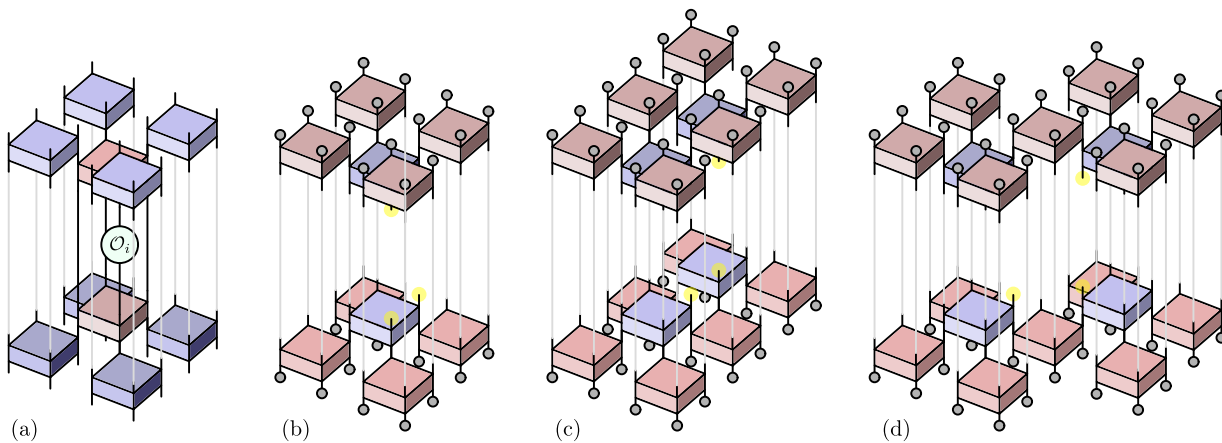


FIG. 5. (a) Illustration of  $U^\dagger \mathcal{O}_i U$  of a local operator  $\mathcal{O}_i$  acting on site  $i$ . Using unitarity,  $U^\dagger \mathcal{O}_i U$  has non-trivial support only in the causal cone of operator  $\mathcal{O}_i$ . (b-d) Diagrammatic representations of the two-site reduced density matrix  $\rho_{ij} = \text{Tr}_{\bar{i}\bar{j}}(|\psi\rangle\langle\psi|)$ . Different choices of the sites  $i$  and  $j$  lead to causal cones of size (b)  $4 \times 4$ , (c)  $4 \times 6$ , and (d) 28 sites. Note that these diagrams are inverted: the top tensor network is  $\langle\psi|$  and the bottom tensor network is  $|\psi\rangle$ . For clarity, the tensor contractions are shown with light gray lines, and the gray circles pinned to the outer legs indicate that these indices are fixed to particular values and hence no longer open. The open tensor legs (on sites  $i$  and  $j$ ) are highlighted in yellow. Note that here we depict the case where the distance  $|i - j|$  is 1, 1, and  $\sqrt{2}$  in (b), (c), and (d) respectively, but different choices of  $i$  and  $j$  lead to the same types of tensor contractions. In particular,  $|i - j|$  can be up to  $\sqrt{2}$  in case (b),  $\sqrt{10}$  in case (c), and  $3\sqrt{2}$  in case (d).

Hilbert space; in this case, the columns of  $U$  are the approximate eigenstates. In the tensor network picture, we adopt the convention where the upper indices are the row indices (or contravariant/“ket” indices) and the lower indices are the column indices (or covariant/“bra” indices). Thus to extract a particular approximate eigenstate from  $U$ , one fixes all the lower indices to particular values: the resulting tensor network has only upper open indices and is a projected entangled pair state (PEPS). The indices take the values  $\{0, c, d\}$ , corresponding to the states  $|0\rangle$ ,  $|c\rangle$ , and  $|d\rangle$ , which span the single-site Hilbert space.

Crucially,  $U$  is unitary, and also conserves particle number, i.e. each approximate eigenstate is of a definite number of clean and dirty particles. In our numerics, these conditions are enforced on the individual tensors in the network [boxes in Fig. 1(c)], which we call  $u$ . (Note that, in general, all tensors are different, as the system is not translationally invariant; here  $u$  refers to a generic one of them.)

To impose particle number conservation, each  $u$  is subject to the condition that the element  $u_{\alpha',\beta',\gamma',\delta'}^{\alpha,\beta,\gamma,\delta}$  is nonzero only if  $\alpha, \beta, \gamma, \delta = \alpha', \beta', \gamma', \delta'$  up to permutation. That is, the four upper indices of  $u$  must contain the same number of both  $c$ 's and  $d$ 's as the four lower indices.  $u$  is also unitary, or more specifically, real and orthogonal—it suffices to have a real ansatz since the Hamiltonian is real. This is imposed by setting  $u = e^M$ , where  $M$  is a real anti-symmetric matrix that contains the actual variational parameters.

The quantum circuit structure of  $U$  ensures that calculations involving local operators are local tensor network contractions of finite range, independent of the overall system size. For example, consider the quantity  $U^\dagger \mathcal{O}_i U$ ,

where  $\mathcal{O}_i$  is a single-site operator acting on site  $i$ . On sites away from  $i$ , the  $u$  and  $u^\dagger$  tensors will cancel due to unitarity. Thus, to calculate  $U^\dagger \mathcal{O}_i U$ , one only needs to consider a  $4 \times 4$  causal cone of the local operator  $\mathcal{O}_i$  as depicted in Fig. 5(a).

### Cost function

We perform the variational diagonalization by minimizing a cost function, which can be motivated by the concept of local integrals of motion (LIOMs) [38–46], also known as l-bits. MBL systems are known to possess a set of LIOMs  $\{\tau_i\}$ , that (in two dimensions approximately [47]) commute with the Hamiltonian and each other, i.e.  $[H, \tau_i] = [\tau_i, \tau_j] = 0$ . Each  $\tau_i$  is an operator that is localized around site  $i$ , and is defined by  $\tau_i = U_{\text{exact}} \sigma_i^z U_{\text{exact}}^\dagger$  for the case of spin-1/2 spin models such as the “standard” disordered Heisenberg model [3, 4, 48], or analogously otherwise.  $U_{\text{exact}}$  is the local unitary operator that diagonalizes the Hamiltonian. Here we define a set of *approximate* LIOMs given by  $\tilde{\tau}_{i,\mu}(U) = U n_{i,\mu} U^\dagger$ , where  $\mu = c, d$ , and  $U$  is the variational quantum circuit. To optimize  $U$ , we define a cost function  $f \propto \sum_{i,\mu} \|[H, \tilde{\tau}_{i,\mu}]\|^2$  that penalizes the non-commutation of  $H$  and  $\tilde{\tau}_{i,\mu}$ . (The  $\tilde{\tau}_{i,\mu}$  already commute with each other by construction.) Thus, by minimizing the cost function we are optimizing the approximate LIOMs. We note that although the motivation was physical, it is also possible to mathematically justify this choice of cost function by showing from the definition of  $\tilde{\tau}_{i,\mu}$  that  $[H, \tilde{\tau}_{i,\mu}] = 0$  for all  $\tilde{\tau}_{i,\mu}$  if and only if  $U H U^\dagger$  is diagonal.

Specifically, the cost function  $f(U)$  is given by

$$f(U) = \frac{1}{2L^2 3L^2} \sum_i \sum_{\mu=c,d} \text{Tr}([H, \tilde{\tau}_{i,\mu}]^\dagger [H, \tilde{\tau}_{i,\mu}])$$

$$= \frac{1}{L^2 3L^2} \sum_i \sum_{\mu=c,d} [\text{Tr}(H^2(\tilde{\tau}_{\mu,i})^2) - \text{Tr}((H\tilde{\tau}_{i,\mu})^2)],$$
(A1)

where the factor of  $1/2L^2 3L^2$  has been included so that  $f(U)$  is an  $\mathcal{O}(1)$  number. Importantly,  $f(U)$  is a sum of quantities that only involve local causal cone calculations, so the total computational cost scales linearly with the system size. For further details on the calculation, we refer the reader to Refs. [21, 22], where a similar optimization procedure was employed.

## Appendix B: Reduced density matrix calculations

Here we describe how we calculate the one- and two-site reduced density matrices from the approximate eigenstates in the optimized  $U$  and how we then use these to obtain the correlation functions and correlation lengths.

Let  $|\psi\rangle$  be a (randomly selected) approximate eigenstate. The setup of our ansatz as a unitary quantum circuit allows us to obtain the single-site density matrix  $\rho_i = \text{Tr}_{\bar{i}}(|\psi\rangle\langle\psi|)$  and two-site density matrix  $\rho_{ij} = \text{Tr}_{\bar{ij}}(|\psi\rangle\langle\psi|)$  via causal cone calculations. However, the two-site density matrix trivially decomposes as  $\rho_{ij} = \rho_i \otimes \rho_j$  unless sites  $i$  and  $j$  have overlapping causal cones, which implies

that one site must lie in a  $6 \times 6$  region around the other. Thus, for each site  $i$  we consider all 35 other sites  $j$  for which nontrivial correlations can be calculated. In Fig. 5 we illustrate the tensor network contractions required to calculate  $\rho_{ij}$  in various cases. The calculation of  $\rho_i$  involves a diagram that is the same as Fig. 5(b), but with open legs on only one site  $i$ .

Due to the square lattice geometry, the distances considered are (in units of the lattice spacing)

$$|i - j| = 1, \sqrt{2}, 2, \sqrt{5}, 2\sqrt{2}, 3, \sqrt{10}, \sqrt{13}, 3\sqrt{2}$$

$$\approx 1, 1.41, 2, 2.23, 2.83, 3, 3.16, 3.61, 4.24. \quad (\text{B1})$$

From the single-site reduced density matrices, we can calculate the on-site entanglement entropies  $S_i = -\text{Tr}(\rho_i \ln \rho_i)$ . From the two site density matrices, we can calculate  $S_{ij} = -\text{Tr}(\rho_{ij} \ln \rho_{ij})$  and thus the quantum mutual information (QMI) between sites. We also calculate the two-point correlation functions, which are defined as

$$C_{\sigma\mu}(i, j) = \langle n_{i,\sigma} n_{j,\mu} \rangle - \langle n_{i,\sigma} \rangle \langle n_{j,\mu} \rangle, \quad (\text{B2})$$

where  $\langle \dots \rangle = \langle \psi | \dots | \psi \rangle$ , so  $\langle n_{i,\sigma} \rangle = \text{Tr}(\rho_i n_\sigma)$  and  $\langle n_{i,\sigma} n_{j,\mu} \rangle = \text{Tr}(\rho_{ij} (n_\sigma \otimes n_\mu))$ , and where  $\sigma, \mu \in \{c, d\}$ . We then calculate  $C_{\sigma\mu}(i, j)$  at various points and perform an exponential fit  $C_{\sigma\mu}(i, j) \propto \exp(-|i - j|/\xi_{\sigma\mu})$  to obtain the correlation length  $\xi_{\sigma\mu}$ . Note that here  $C_{\sigma\mu}$  and hence  $\xi_{\sigma\mu}$  corresponds to a specific eigenstate. We average over eigenstates and disorder realizations to obtain the average quantities  $\bar{C}_{\sigma\mu}(\Delta)$  and  $\bar{\xi}_{\sigma\mu}(\Delta)$  at a given disorder strength  $\Delta$ .

- 
- [1] I. V. Gornyi, A. D. Mirlin, and D. G. Polyakov, Interacting electrons in disordered wires: Anderson localization and low-T transport, *Phys. Rev. Lett.* **95**, 206603 (2005).
- [2] D. M. Basko, I. L. Aleiner, and B. L. Altshuler, Metal-insulator transition in a weakly interacting many-electron system with localized single-particle states, *Ann. Phys.* **321**, 1126 (2006).
- [3] M. Žnidarič, T. Prosen, and P. Prelovšek, Many-body localization in the Heisenberg XXZ magnet in a random field, *Phys. Rev. B* **77**, 064426 (2008).
- [4] A. Pal and D. A. Huse, Many-body localization phase transition, *Phys. Rev. B* **82**, 174411 (2010).
- [5] M. Schreiber, S. S. Hodgman, P. Bordia, H. P. Lüschen, M. H. Fischer, R. Vosk, E. Altman, U. Schneider, and I. Bloch, Observation of many-body localization of interacting fermions in a quasirandom optical lattice, *Science* **349**, 842 (2015).
- [6] J. Smith, A. Lee, P. Richerme, B. Neyenhuis, P. W. Hess, P. Hauke, M. Heyl, D. A. Huse, and C. Monroe, Many-body localization in a quantum simulator with programmable random disorder, *Nat. Phys.* **12**, 907 (2016).
- [7] S. Choi, J. Choi, R. Landig, G. Kucsko, H. Zhou, J. Isoya, F. Jelezko, S. Onoda, H. Sumiya, V. Khemani, C. von Keyserlingk, N. Y. Yao, E. Demler, and M. D. Lukin, Observation of discrete time-crystalline order in a disordered dipolar many-body system, *Nature* **543**, 221 (2017).
- [8] P. Roushan, C. Neill, J. Tangpanitanon, V. M. Bastidas, A. Megrant, R. Barends, Y. Chen, Z. Chen, B. Chiaro, A. Dunsworth, *et al.*, Spectroscopic signatures of localization with interacting photons in superconducting qubits, *Science* **358**, 1175 (2017).
- [9] A. Lukin, M. Rispoli, R. Schittko, M. E. Tai, A. M. Kaufman, S. Choi, V. Khemani, J. Léonard, and M. Greiner, Probing entanglement in a many-body-localized system, *Science* **364**, 256 (2019).
- [10] J. Z. Imbrie, On many-body localization for quantum spin chains, *J. Stat. Phys.* **163**, 998 (2016).
- [11] J. Šuntajs, J. Bonča, T. Prosen, and L. Vidmar, Quantum chaos challenges many-body localization, *Phys. Rev. E* **102**, 062144 (2020).
- [12] D. Sels and A. Polkovnikov, Dynamical obstruction to localization in a disordered spin chain, *Phys. Rev. E* **104**, 054105 (2021).
- [13] J. C. Peacock and D. Sels, Many-body delocalization from embedded thermal inclusion, *Phys. Rev. B* **108**, L020201 (2023).
- [14] W. D. Roeck and J. Z. Imbrie, Many-body localization: stability and instability, *Phil. Trans. R. Soc. A* **375**,

- 20160422 (2017).
- [15] S. Gopalakrishnan and D. A. Huse, Instability of many-body localized systems as a phase transition in a non-standard thermodynamic limit, *Phys. Rev. B* **99**, 134305 (2019).
- [16] J.-y. Choi, S. Hild, J. Zeiher, P. Schauß, A. Rubio-Abadal, T. Yefsah, V. Khemani, D. A. Huse, I. Bloch, and C. Gross, Exploring the many-body localization transition in two dimensions, *Science* **352**, 1547 (2016).
- [17] A. Rubio-Abadal, J.-y. Choi, J. Zeiher, S. Hollerith, J. Rui, I. Bloch, and C. Gross, Many-Body Delocalization in the Presence of a Quantum Bath, *Phys. Rev. X* **9**, 041014 (2019).
- [18] F. Pollmann, V. Khemani, J. I. Cirac, and S. L. Sondhi, Efficient variational diagonalization of fully many-body localized Hamiltonians, *Phys. Rev. B* **94**, 041116(R) (2016).
- [19] T. B. Wahl, A. Pal, and S. H. Simon, Efficient Representation of Fully Many-Body Localized Systems Using Tensor Networks, *Phys. Rev. X* **7**, 021018 (2017).
- [20] T. B. Wahl, F. Venn, and B. Béri, Local integrals of motion detection of localization-protected topological order, *Phys. Rev. B* **105**, 144205 (2022).
- [21] T. B. Wahl, A. Pal, and S. H. Simon, Signatures of the Many-body Localized Regime in Two Dimensions, *Nat. Phys.* **15**, 164 (2019).
- [22] J. Li, A. Chan, and T. B. Wahl, Quantum circuits reproduce the experimental two-dimensional many-body localization transition point, *Phys. Rev. B* **109**, L140202 (2024).
- [23] F. Venn, T. B. Wahl, and B. Béri, Many-body-localization protection of eigenstate topological order in two dimensions, arXiv:2212.09775, to appear in *Phys. Rev. B*.
- [24] T. B. Wahl, Tensor networks demonstrate the robustness of localization and symmetry-protected topological phases, *Phys. Rev. B* **98**, 054204 (2018).
- [25] A. Chan and T. B. Wahl, Classification of symmetry-protected topological many-body localized phases in one dimension, *J. Phys.: Cond. Mat.* **32**, 305601 (2020).
- [26] J. Li, A. Chan, and T. B. Wahl, Classification of symmetry-protected topological phases in two-dimensional many-body localized systems, *Phys. Rev. B* **102**, 014205 (2020).
- [27] H. Ha, A. Morningstar, and D. A. Huse, Many-Body Resonances in the Avalanche Instability of Many-Body Localization, *Phys. Rev. Lett.* **130**, 250405 (2023).
- [28] J. A. Kjäll, J. H. Bardarson, and F. Pollmann, Many-body localization in a disordered quantum Ising chain, *Phys. Rev. Lett.* **113**, 107204 (2014).
- [29] D. Hundertmark, *A short introduction to Anderson localization* (Analysis and stochastics of growth processes and interface models, 2008) pp. 194–218.
- [30] F. Pietracaprina, V. Ros, and A. Scardicchio, Forward approximation as a mean-field approximation for the Anderson and many-body localization transitions, *Phys. Rev. B* **93**, 054201 (2016).
- [31] A. Scardicchio and T. Thiery, Perturbation theory approaches to Anderson and Many-Body Localization: some lecture notes, arXiv:1710.01234.
- [32] G. De Tomasi, S. Bera, J. H. Bardarson, and F. Pollmann, Quantum mutual information as a probe for many-body localization, *Phys. Rev. Lett.* **118**, 016804 (2017).
- [33] B. Villalonga and B. K. Clark, Characterizing the many-body localization transition through correlations (2020), arXiv:2007.06586 [cond-mat.dis-nn].
- [34] A. Morningstar, L. Colmenarez, V. Khemani, D. J. Luitz, and D. A. Huse, Avalanches and many-body resonances in many-body localized systems, *Phys. Rev. B* **105**, 174205 (2022).
- [35] V. Khemani, S. P. Lim, D. N. Sheng, and D. A. Huse, Critical properties of the many-body localization transition, *Phys. Rev. X* **7**, 021013 (2017).
- [36] B. Villalonga and B. K. Clark, Eigenstates hybridize on all length scales at the many-body localization transition, arXiv:2005.13558 (2020).
- [37] P. Crowley and A. Chandran, A constructive theory of the numerically accessible many-body localized to thermal crossover, *SciPost Physics* **12**, 201 (2022).
- [38] M. Serbyn, Z. Papić, and D. A. Abanin, Local Conservation Laws and the Structure of the Many-Body Localized States, *Phys. Rev. Lett.* **111**, 127201 (2013).
- [39] D. A. Huse, R. Nandkishore, and V. Oganesyan, Phenomenology of fully many-body-localized systems, *Phys. Rev. B* **90**, 174202 (2014).
- [40] A. Chandran, I. H. Kim, G. Vidal, and D. A. Abanin, Constructing local integrals of motion in the many-body localized phase, *Phys. Rev. B* **91**, 085425 (2015).
- [41] V. Ros, M. Müller, and A. Scardicchio, Integrals of motion in the many-body localized phase, *Nucl. Phys. B* **891**, 420 (2015).
- [42] S. Inglis and L. Pollet, Accessing Many-Body Localized States through the Generalized Gibbs Ensemble, *Phys. Rev. Lett.* **117**, 120402 (2016).
- [43] L. Rademaker and M. Ortuño, Explicit Local Integrals of Motion for the Many-Body Localized State, *Phys. Rev. Lett.* **116**, 010404 (2016).
- [44] C. Monthus, Many-body localization: construction of the emergent local conserved operators via block real-space renormalization, *J. Stat. Mech.* **2016**, 033101 (2016).
- [45] M. Goihl, M. Gluza, C. Krumnow, and J. Eisert, Construction of exact constants of motion and effective models for many-body localized systems, *Phys. Rev. B* **97**, 134202 (2018).
- [46] A. K. Kulshreshtha, A. Pal, T. B. Wahl, and S. H. Simon, Behavior of l-bits near the many-body localization transition, *Phys. Rev. B* **98**, 184201 (2018).
- [47] A. Chandran, A. Pal, C. R. Laumann, and A. Scardicchio, Many-body localization beyond eigenstates in all dimensions, *Phys. Rev. B* **94**, 144203 (2016).
- [48] D. J. Luitz, N. Laflorencie, and F. Alet, Many-body localization edge in the random-field Heisenberg chain, *Phys. Rev. B* **91**, 081103 (2015).